Journal of Environmental Chemical Engineering 13 (2025) 117541

Contents lists available at ScienceDirect

Journal of Environmental Chemical Engineering

journal homepage: www.elsevier.com/locate/jece

Synthesis of high entropy, bidimensional mixed oxides from multimetallic layered double hydroxide precursors and application in photocatalytic N_2 hydrogenation to ammonia

Manuel Molina-Muriel [a,b], Adrián Pastor [a,c], Fernando Déniz [b], Antonio Ribera [b,*], Hermenegildo García [a]

[a] Instituto de Tecnología Química CSIC-UPV, Universitat Politècnica de València and Consejo Superior de Investigaciones Científicas, Universitat Politècnica de València, Av. de los Naranjos s/n, Valencia 46022, Spain
[b] Departamento de Química Inorgánica, Universitat de València, Carrer del Doctor Moliner, 50, Valencia, Burjassot 46100 Spain.
[c] Departamento de Química Inorgánica, Instituto de Química para la Energía y Medioambiente, Universidad de Córdoba, Campus de Rabanales, Córdoba E-14014, Spain

ARTICLE INFO

Keywords:
High-entropy oxides
Layered double hydroxides
N_2 hydrogenation
Ammonia production
Photocatalysis
High-entropy materials

ABSTRACT

A multimetallic layered double hydroxide containing seven metals has been prepared by coprecipitation in DMF/H_2O at pH 10 and converted into a seven metal mixed oxide. This high-entropy mixed metal (HE-MO) inherits from the LDH precursor the hexagonal sheet morphology. High resolution transmission electron microscopy, and EDS elemental mapping convincingly proves the absence of segregation of some elements in a different phase. Remarkably, neither noble metals nor lanthanides are used during the synthesis, and no reduction processes are needed to obtain the HE-MO. The resulting HE-MO promotes under continuous flow the photocatalytic nitrogen hydrogenation at atmospheric pressure and 200 °C with UV–vis light (108 mW cm^{-2}) at a rate of 20 μmol $NH_3 \cdot g^{-1} \cdot h^{-1}$, lower or higher temperatures resulting in lower rates. This NH_3 rate formation is much higher than that of a CoFe mixed oxide reference or than values reported in the literature for noble metal-free photocatalysts. The use of isotopically labelled $^{15}N_2$ firmly proves this gas is the origin of the formed NH_3. Influence of the N_2 and H_2 proportion shows that the rate determining step is the generation of active H species on the photocatalyst surface, while the photoresponse derives from the UV region. Photoluminescence measurements indicate the existence of a transient state of charge separation responsible for the photocatalytic reaction.

1. Introduction

Metal oxides, such as TiO_2, ZnO, WO_3, CeO_2 and others, are among the best studied photocatalysts[1–4]. The presence of a second metal in their structure has frequently been reported to be beneficial for their photocatalytic activity[5–7], given that, when two metals are present in a semiconductor, the density of states becomes more complex allowing the introduction of intra bandgap states that modify the optoelectronic properties and performance of the bimetallic material[8]. Similar beneficial effect as the introduction of a second metal in photocatalysis has been also observed in materials used as thermal catalysts[9,10], electrocatalysts[11,12] and in other applications, such as capacitance [13] and magnetism[14]. A logical extension of this property tunability observed in bimetallic oxides could occur upon introduction of a third, fourth or further metals.

In the case of materials containing elements in the metallic oxidation state, the presence of five or more metallic elements in similar proportions has led to the concept of high-entropy alloys, with unbeatable properties[15,16]. Analogously, it can be assumed that the presence of many metallic elements in metal oxides should be considered as a powerful tool to optimize the performance of the resulting mixed oxide for a particular application, and more specifically in photocatalysis [17–19]. A key issue to overcome in the preparation of multimetallic metal oxides is the segregation of different separate crystal phases, since the objective to be achieved is a material containing simultaneously all the elements present in the precursors in a single crystalline phase[20].

In this context, layered double hydroxides (LDH) stand out as suitable precursors for the preparation of these monophasic mixed oxides containing a plethora of different metallic elements[21–23]. LDHs contain typically two metal elements in M^{2+} and M^{3+} oxidation state

* Corresponding author.
E-mail address: antonio.ribera@uv.es (A. Ribera).

https://doi.org/10.1016/j.jece.2025.117541
Received 5 March 2025; Received in revised form 28 May 2025; Accepted 9 June 2025
Available online 10 June 2025

and have a 2D morphology consisting in stacking layers of octahedra [24]. The presence of a tri-positive metal cation replacing isomorphically the M^{2+} metal ion introduces a net positive charge in the layer that requires the presence of counter balancing anions occupying intergallery positions. In the area of LDH synthesis, a current trend is the introduction of a third, and even a fourth metal element, in some cases with a coulombic charge different from + 2 and + 3[25,26]. Following this trend, the preparation procedure of LDH could allow the formation of *high-entropy* LDHs that, in turn, could be used as precursors for the synthesis of single-phase, *high-entropy* mixed oxides. Although there are a few scarce reported precedents of multimetallic LDHs[27–29], the exploration of the possible applications of this kind of materials in photocatalysis remains unexplored.

Herein, we report the preparation of an LDH containing seven different di-positive and tri-positive metallic elements in a single phase with sheet morphology. Upon thermal treatment, this multimetallic LDH becomes converted into a 2D multimetallic, single-phase oxide that has been used as photocatalyst for the light-assisted nitrogen hydrogenation at atmospheric pressure as probe reaction. Comparison of the performance of this heptametallic mixed oxide with the corresponding bimetallic CoFe mixed oxide prepared by the same procedure clearly shows the advantage as photocatalyst of the material having a multimetallic composition. Therefore, our results open a new avenue for the application of novel bidimensional multimetallic mixed oxides in photocatalysis, with enhanced properties respect to mono- or bimetallic analogs.

2. Experimental section

2.1. Materials

$Fe(NO_3)_3{\cdot}9H_2O$ and NH_4Cl were purchased from Alfa-Aesar. $Zn(NO_3)_2{\cdot}6H_2O$, $Co(NO_3)_2{\cdot}6H_2O$, $Mg(NO_3)_2{\cdot}6H_2O$, $Ga(NO_3)_3{\cdot}xH_2O$, $In(NO_3)_3{\cdot}xH_2O$, $Fe(NO_3)_3{\cdot}9H_2O$, $Al(NO_3)_3{\cdot}9H_2O$, $CaCl_2$, N,N-dimethylformamide (DMF), ethanol (EtOH), terpineol, acetone, phenol, sodium nitrate and sodium nitroprusside were obtained from Sigma-Aldrich. Water used in all experiments was milliQ purity grade.

2.2. Catalyst preparation

For the synthesis of a high-entropy mixed oxide (HE-MO) containing seven metals a modified procedure from the literature that yields LDH with a low degree of layer stacking was applied[30]. In brief, 0.33 g (1.1 mmol) of $Zn(NO_3)_2{\cdot}6H_2O$, 0.33 g (1.1 mmol) of $Co(NO_3)_2{\cdot}6H_2O$, 0.29 g (1.1 mmol) of $Mg(NO_3)_2{\cdot}6H_2O$, 0.16 g (0.4 mmol) of $Al(NO_3)_3{\cdot}9H_2O$, 0.11 g (0.4 mmol) of $Ga(NO_3)_3{\cdot}xH_2O$, 0.13 g (0.4 mmol) of $In(NO_3)_3{\cdot}xH_2O$ and 0.17 g (0.4 mmol) of $Fe(NO_3)_3{\cdot}9H_2O$ were dissolved in 50 ml of distilled water. 20 ml of the above solution were added dropwise with the help of an infusion pump (10 min, 120 $ml{\cdot}h^{-1}$ flow rate) over 20 ml of a 23 vol% DMF aqueous solution at 80 ºC, maintaining the pH at 10 during the process with the addition of 0.25 M NaOH with a potentiometric titrator. The originated suspension after the complete addition was cooled down in an ice bath and centrifuged at 5000 rpm for 10 min, washing 3 times with an EtOH:H_2O 1:1 mixture. The recovered solid (labelled as HE-LDH) was dried in a desiccator under vacuum. Finally, in order to get the corresponding high-entropy mixed oxide (HE-MO), the HE-LDH powder was placed in a crucible and calcined in a muffle furnace at 400 ºC under air atmosphere for 6 h (heating and cooling down ramps were 1 $ºC{\cdot}min^{-1}$). As a reference, a bimetallic LDH containing Co and Fe (named as CoFe-LDH) was prepared using the same procedure, with the metallic precursor solution containing 0.98 g (3.3 mmol) of $Co(NO_3)_2{\cdot}6H_2O$ and 0.69 g (1.7 mmol) of $Fe(NO_3)_3{\cdot}9H_2O$ in 50 ml of distilled water. CoFe-LDH calcination under identical conditions yielded the CoFe-MO compound.

2.3. Materials characterization

Powder X-ray diffraction (PXRD) measurements were conducted in a Philips X'PERT diffractometer, operating at 40 kV and 45 mA, equipped with a graphite monochromator and using Cu Kα (λ = 1.54178 Å) irradiation. Data were collected in the 2θ range 5–90 º. In situ PXRD measurements were performed on a PANanalytical EMPYREAN diffractometer equipped with a high temperature chamber (Anton Paar XRK-900). During the experiments, a gas flow of 10 % H_2 in Ar (60 $ml{\cdot}min^{-1}$) was circulated through the sample chamber. Data were collected with a PIXcel1D-Medipix3 detector, with a Ni filter in the diffracted beam, and using Cu Kα irradiation (λ_1 = 1.5406 Å, λ_2 = 1.5444 Å, I_2/I_1 = 0.5), operating at 45 kV and 40 mA. Signals were monitored in the range 2θ = 5–90 º at different temperatures (25, 100, 200, 300, 400 ºC, and finally after cooling down the system to room temperature). Thermogravimetric analysis (TGA) was done in a Metter Toledo TGA/SDTA 85 (25–800 °C, heating rate = 10 $°C{\cdot}min^{-1}$, air).

Field-emission scanning electron microscopy (FESEM) images and EDX data were obtained on a Zeiss Ultra 55 apparatus, equipped with an EDX detector. Transmission electron microscopy (TEM), high angle annular dark-field scanning transmission electron microscopy (HAADF-STEM) images, and elemental mapping of the material were collected on a JEOL JEM 2100 F electronic microscope also equipped with an EDX detector. X-ray photoelectron spectroscopy (XPS) data were obtained on a SPECS spectrometer equipped with a PHOIBOS 150 MCD-9 detector, employing a non-monochromatic radiation source (Al), and operating a 200 W. First, samples were pretreated under vacuum ($1{\cdot}10^{-9}$ mbar) in the prechamber of the equipment. Deconvolution of the experimental data was carried out with the help of CASA XPS software. The obtained spectra were calibrated against adventitious carbon C 1 s peak at 284.6 eV.

Inductively coupled plasma optical emission spectroscopy (ICP-OES) was measured in a Varian 715-ES ICP Optical Emission Spectrometer, after dissolving 30 mg of sample in around 8 ml HCl:HNO 3:1 filtering and making up to 30 ml with Milli-Q water. Diffuse reflectance UV-Vis spectroscopy (UV-DRS) data were registered on a PerkinElmer Lambda 1050 spectrophotometer equipped with a Harrick Praying Mantis™ DRS accessory. The valence band region of XPS and ultraviolet photoelectron spectroscopy (UPS) spectra were obtained using a PHI 5000 Versaprobe II (Physical Electronics). For UPS, a He 1 UV source with an energy of 21.22 eV at 50.0 W was used, and the sample was tilted 90° relative to the analyzer. The sample was cleaned by sputtering with Ar^+ at a low energy of 500 V. A bias voltage of −5 V was applied. The binding energy scale was calibrated using the Fermi level measured on a polycrystalline gold foil. H_2 temperature programmed reduction (H_2-TPR) measurements were conducted on a Micromeritics Autochem 2910 apparatus, in the temperature range of 40–800 ºC, with a heating rate of 10 $ºC{\cdot}min^{-1}$ and under a 10 % of H_2 in Ar (50 $ml{\cdot}min^{-1}$) gas flow. Steady-state fluorescence emission spectra of the solid was recorded on an Edinburgh Instruments FLS1100 spectrophotometer equipped with double grating Czerny-Turner monochromators with 2 × 325 focal length in excitation and detection, and a PMT-980 detector in the range 200–980 nm. The study consisted in a scan of the emission spectra at different excitation wavelengths on intervals of 20 nm in the range 290–900 nm. A 400 W Xe lamp was employed as a light source for the excitation. Time Resolved Photoluminescence (TRPL) was performed on an Edinburgh Instruments FLS1100 spectrophotometer by excitation at 364.2 nm with a diode (EPLED-365, Edinburgh). Photocurrent measurements were carried out on a potentiostat/galvanostat (Interface 5000E, Gamry Instruments). The electrochemical cell consisted of a 0.1 M Na_2SO_4 aqueous solution (electrolyte) and three electrodes inside a sealed quartz cell: Pt wire (counter electrode), Ag/AgCl (reference electrode) and a working electrode. The working electrode was prepared by casting a suspension of the photocatalyst onto 1 cm^2 of FTO glasses. Specifically, the suspension was prepared by mixing 0.5 ml of acetone, 0.25 ml of terpineol and 37.5 mg of photocatalyst. The suspension was

placed into a sealed vial, sonicated for 2 h, stirred overnight, and finally the vial was opened and heated (70 °C) to allow some evaporation for around 6 h, obtaining a viscous ink. Subsequently, the ink was casted onto the FTOs and dried at 120 °C for 1 h. A 300 W Xe lamp equipped with an optical fibre was used as a light source, measuring the transient photocurrent by turning the lamp on/off while applying a bias of + 1 V.

2.4. Photocatalytic tests

Continuous flow photocatalytic hydrogenation of N_2 was carried out on a home-built fixed-bed tubular reactor operating at ambient pressure. The catalyst bed (50 mg, 10 mm diameter and approximately 1 mm thickness) was supported on a porous quartz frit inside a vertical quartz tube. The reactor was heated by a heating mantle surrounding it, while the temperature is controlled by a type κ thermocouple. The dead volume in the system before the catalytic bed was enough to ensure the heating of the inlet circulating gas before being in contact with the photocatalyst. The sample was irradiated from the top of the reactor using the output of a 300 W Xe lamp (108 mW·cm^{-2}) through an optical fiber (spot size 10 mm^2) inserted in the quartz tube to ensure the uniform irradiation of the sample. A schematic diagram of the system is presented in Scheme S1.

To rule out any possible contamination of NH_3 in the feed, the inlet gas was bubbled through a flask containing a 0.5 mM H_2SO_4 aqueous solution, then through water to clean the acid, and through a column filled with $CaCl_2$ as desiccant. To collect the produced ammonia, the outlet gas of the reactor was bubbled through two consecutive flasks, each one containing 5 ml of a 0.5 mM H_2SO_4 aqueous solution. The second flask served as confirmation that all the produced ammonia was trapped in the first one. Ammonia was quantified using blue indophenol method[31] (see more details in Supporting Information).

Before irradiation, the system was pretreated under H_2 flow (30 ml·min^{-1}) at the same temperature of the subsequent catalytic test (100, 150, 200, 250 or 350 ºC) during 1 h. After the activation, a gas flow of N_2/H_2 (10 ml·min^{-1} and 30 ml·min^{-1}, respectively) was circulated through the reactor, irradiating at the same time with the output of a 300 W Xe lamp. The solutions from flasks 1 and 2 were collected for total ammonia quantification after 30 min reaction.

To study the behavior of the photocatalyst under different reaction conditions, experiments where the temperature, flow of one of the gases, or the wavelength of the incident light (with the use of band-pass filters) were modified, were performed. In addition, to check that the produced ammonia is not originated from impurities or contamination, both in the catalyst or in the gas flow, two control experiments, one using an Ar flow instead of N_2 and a second one employing labelled $^{15}N_2$ as the feeding gas, were carried out. For the $^{15}N_2$ experiment, a customized batch quarz photoreactor was used in order to increase the concentration of labeled $^{15}NH_3$ allowing quantification by ^{1}H NMR spectroscopy. Specifically, the reactor was purged with H_2, filled with $^{15}N_2$ and H_2 at 1:3 molar ratio and allowed to react for 90 h under the same temperature, pressure and light irradiation than used for the continuous flow set-up (200° C, Xe lamp irradiation, 108 mW·cm^{-2}). Upon reaction, the outlet of the reactor was connected to two consecutive acid reservoirs as indicated in Scheme S1. Then, the outlet of the reactor was open to trap the generated NH_3 into the acid reservoir. Finally, the reactor was thoroughly purged with Ar for 20 min while keeping the acid reservoirs connected. $^{15}NH_3$ trapped in reservoir 1 was analyzed by 400 MHz ^{1}H NMR spectroscopy. Perdeuterated dimethylsulfoxide (DMSO-d_6) and dried acetonitrile (CH_3CN) were used as reference and internal standard, respectively.

3. Results and discussion

3.1. Materials synthesis and characterization

To prove the concept of high-entropy LDHs, seven metallic elements were selected. The selection was made to combine elements with presumably structural role like Al and Ga, others to introduce basicity in the metal oxide, such as Mg, others with presumably hydrogenation activity, like Co and Fe, and photocatalytic activity, like Zn and In. Equimolar amounts of the tripositive (1.1 mmol) and dipositive (0.4 mmol) metal cations were used, keeping the total trivalent/divalent atomic ratio within the 2:1 range allowed for LDH synthesis, to avoid phase segregation. Even though the cationic elements present in the structure are not in equimolar amounts, the configurational entropy metric of these systems is included within the entropy range ascribed to high-entropy materials, as it has been already reported for similar systems[32].

The synthesis of heptametallic high-entropy LDH (HE-LDH) was performed by precipitation in a mixture of DMF/H_2O (23 % vol. of DMF) at 80 ºC of an aqueous solution of the corresponding divalent (Mg, Zn, Co) and trivalent (Al, Ga, In, Fe) nitrates by co-injection of an aqueous NaOH solution at pH = 10 maintaining the pH value constant. A key point of the synthetic procedure was the fast addition of the metal solution and the alkali to minimize excessive particle growth, ensuring the production of small LDH sheets. On the other hand, the presence of DMF is known to disfavor the stacking of the sheets in the synthesis of LDH, that are formed with a considerable larger degree of exfoliation[30,33]. After complete mixing of the two solutions a hydrogel was formed, and the suspension was centrifuged and dried. Scheme 1 illustrates the procedure followed for the synthesis of HE-LDH and its corresponding mixed oxide.

At this point, the XRD pattern of the HE-LDH powder indicates the formation of a highly crystalline material (see Fig. 1). In this sense, the pattern is characteristic of LDH compounds, in which the basal reflections (*00 l*) are found below a 2θ value of 30 degrees (these reflections being related to the stacking of the metal-hydroxide layers through the *c*-axis) and the rest of reflections are ascribed to the (*012*) (*015*) (*018*) (*110*) and (*113*) planes[34]. This multimetallic LDH powder was calcined at 400 ºC under air atmosphere to obtain the corresponding multimetallic mixed oxide (HE-MO). Analysis of the XRD of HE-MO indicates that it corresponds to a spinel with low crystallinity (ICCD 00–050–0235)[27]. The mild temperatures used in the calcination process are responsible of the low degree of crystallinity. Higher calcination temperatures would have yielded a more crystalline phase, but producing a collapse of the layered structure at the same time, as it has been previously reported[35].

Fig. S1 showed that the thermal decomposition of the HE-LDH was performed in three steps (weight losses) in the studied range (up to 800 ºC). These weight losses, typical of LDH materials, are ascribed to the desorption of physiosorbed water molecules (30–160 ºC), decomposition of the hydroxyl groups from the metal hydroxide layers (160–280 ºC) and decomposition of interlayer anions and further dehydroxylation (280–800 ºC)[34]. Therefore, the TGA of the HE-LDH indicated its transformation into HE-MO at 400 ºC. For the sake of comparison, a bimetallic mixed oxide only containing Co and Fe was prepared using the same procedure from the corresponding CoFe-LDH. Supporting information (Fig. S2) presents XRD pattern of CoFe-LDH and the corresponding bimetallic mixed oxide.

Chemical analysis by EDX of the high entropy solids clearly establishes the presence of the seven metals in their composition. This composition of the solids is in good agreement with the expected analytical data assuming the complete incorporation in the materials of all the metallic elements used in the synthesis. The results are summarized in Table 1 that also includes chemical analysis for the bimetallic CoFe-LDH and CoFe-MO as reference materials. Correspondingly, the ICP-OES of the HE-MO confirms its composition of the seven metals, in which the error for each element is below 1 % respect to the theoretical value of every metal (Table S1).

One peculiarity of the resulting HE-LDH and, therefore, the corresponding HE-MO, is that the composition exhibits a higher percentage of divalent metals respect to the trivalent ones (Table S1). This preferential composition is derived from the requirements of LDH synthesis that

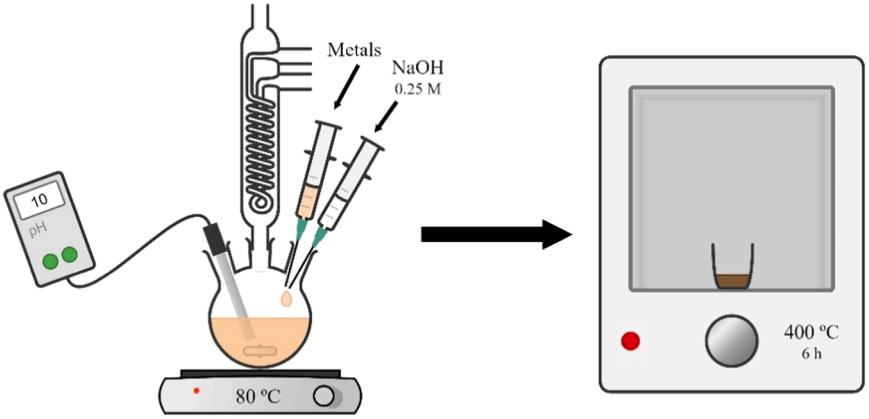

Scheme 1. Synthetic procedure for the preparation of HE-LDH by precipitation in DMF/H_2O at pH 10 and its derived mixed oxide obtained by calcination.

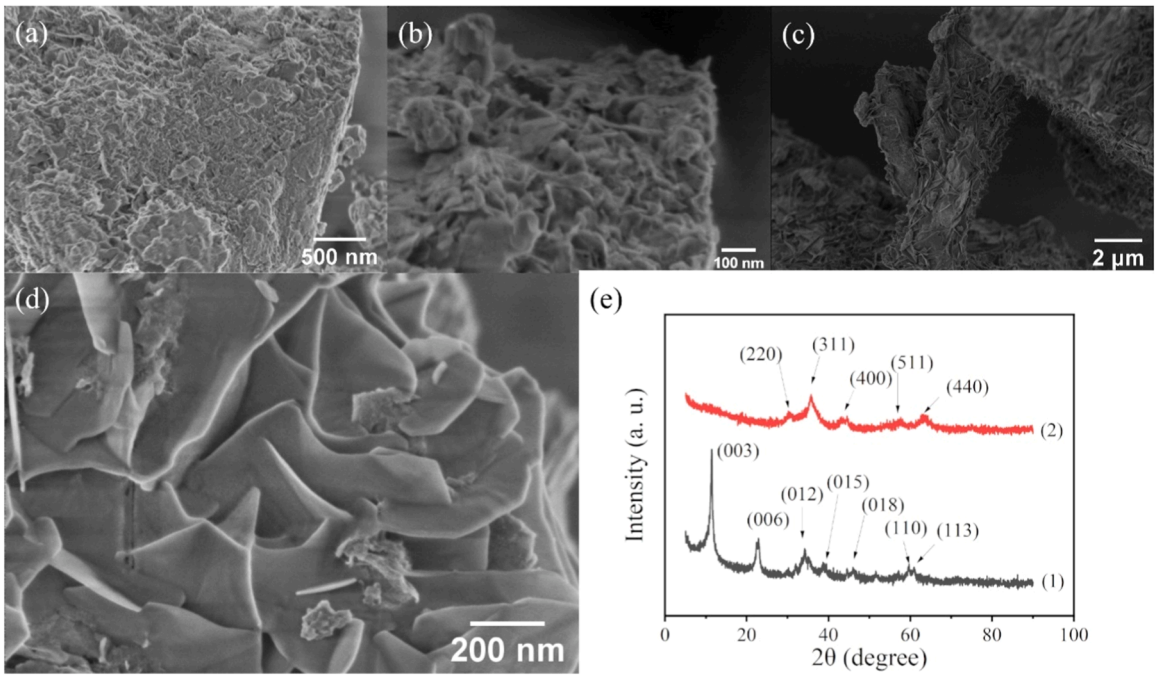

Fig. 1. FESEM images of HE-LDH (a-b) and HE-MO (c-d). XRD patterns (e) of HE-LDH (1) and HE-MO (2).

Table 1
Atomic percentages of the metal elements present in the different materials under study measured by EDX analysis.

	MATERIAL			
	HE-LDH	HE-MO	CoFe-LDH	CoFe-MO
Co (%)	21.8	24.6	67.2	66.0
Zn (%)	24.3	23.5	/	/
Mg (%)	27.0	23.8	/	/
Fe (%)	7.7	8.8	32.8	34.0
Al (%)	9.3	8.4	/	/
Ga (%)	4.2	4.1	/	/
In (%)	5.8	6.8	/	/

limits the percentage of trivalent cations in the LDH sheet to a maximum of about one third of the total metal atoms[21]. This limit in the percentage of trivalent elements avoids the segregation of $M^{III}(OH)_3$ domains, derived from the presence of M^{III}-M^{III} species in close contact, which would occur at percentages above 33 %[24,36]. However, this limitation in the composition is over-compensated by the surprising flexibility that LDH synthesis has to incorporate many different metals, seven in the present case[37].

The 2D morphology of HE-LDH and HE-MO was determined by scanning electron microscopy. FESEM images of HE-LDH show a thick and dense solid constituted by layers of a few microns of lateral size. Notably, upon calcination of HE-LDH, the 2D morphology is preserved and inherited by the resulting multimetallic mixed oxide, whose powder is also formed by the dense agglomeration of 2D sheets. Fig. 1 presents selected images of these multimetallic materials both in the form of LDH or mixed oxide. Also, the control CoFe-LDH and its bimetallic mixed oxide derived therefrom present dense particles where the presence of plates in the micrometer range can be observed (Fig. S3).

The 2D morphology and the crystallinity of the prepared materials is clearly revealed by TEM. In the TEM images of reference materials CoFe-LDH and CoFe-MO, platelets of several hundred nm are observed. Close inspection of some of them show the characteristic hexagonal morphology with 120 ° angles of the sheets as it has been previously observed for well crystallized LDH[38], and that are also preserved in the calcination process. Fig. S4 presents selected images of these CoFe reference materials, in which the presence of these characteristic plates

with hexagonal angles have been highlighted. HRTEM clearly shows crystallinity in the particles with interlayer distances of 0.261 nm and 0.240 nm for CoFe-LDH and CoFe-MO, respectively. These distances correspond well with the (012) facet of LDH structure and (311) plane of spinel-type structure, respectively, and they are in agreement with the X-ray diffraction pattern of these CoFe solids.

In the case of high entropy materials, the presence of a higher number of metals is translated into a lower degree of crystallinity, as observed in the PXRD analysis shown in Fig. 1a. This broader diffraction lines probably reflect the formation of smaller sized sheets for the HE-LDH compared to the reference CoFe-LDH. Nevertheless, platelets with hexagonal morphology can also be observed in the HRTEM images at higher magnification (see Fig. 2).

In the images, interplanar distances of 0.232 nm for (015) planes in HE-LDH, and 0.240 nm for (311) planes in HE-MO, were observed. Furthermore, selected area electron diffraction clearly shows that the sheets are crystalline with a hexagonal diffraction pattern that is well resolved in the case of HE-MO. Therefore, electron microscopy analysis provides a strong support to the presence of a single phase, either LDH or mixed oxide, containing simultaneously the seven metals. Importantly, the presence of nanoparticles or materials with other morphology that could indicate the segregation of some of the elements in separate phases was not observed.

Additional experimental evidence that supports the formation of high entropy materials was obtained by elemental mapping of the sheets by EDX over the STEM images of the samples. A selection of these images is presented in Fig. 3, that shows that for a sheet of 500 nm, the distribution for the seven elements in the particle is coincident, meaning that all the metals are distributed randomly in the sheet.

This elemental mapping, combined with the crystallinity observed in high resolution TEM and the electron diffraction pattern, provided convincing evidence of the formation of the multimetallic materials without separated domains or different particles. This is an important finding that opens the door for preparation of LDH and mixed oxides containing an even larger number of metals with optimized percentages, beyond the equimolar amounts employed in the present study. Furthermore, the synthesis of mixed metal oxides with 2D hexagonal sheet morphology is remarkable, because metal oxides most often tend to form 3D particulate materials.

The presence of the metallic elements on the surface of HE-MO was also determined by XPS. Fig. 4 presents the survey spectra and some of the most representative XPS peaks, as well as the corresponding deconvolution to individual components, while Fig. S5 in the supporting information provides the XPS peaks for the other elements. A general feature of the obtained spectra is the low intensity of the signals, especially in the case of the elements present in smaller ratios. In the case of XPS Co 2p peak, two components at 780.6 and 783.2 eV and a weak satellite peak at 789.6 eV could be observed, typical of Co^{2+} and Co^{3+} oxidation states in Co_3O_4 environment[28]. Although the precursors used for the synthesis for the HE-LDH precursor and HE-MO photocatalyst only contain Co^{2+}, oxidation of Co^{2+} to Co^{3+} is common during the synthesis of LDH materials, as it has been intensively studied by

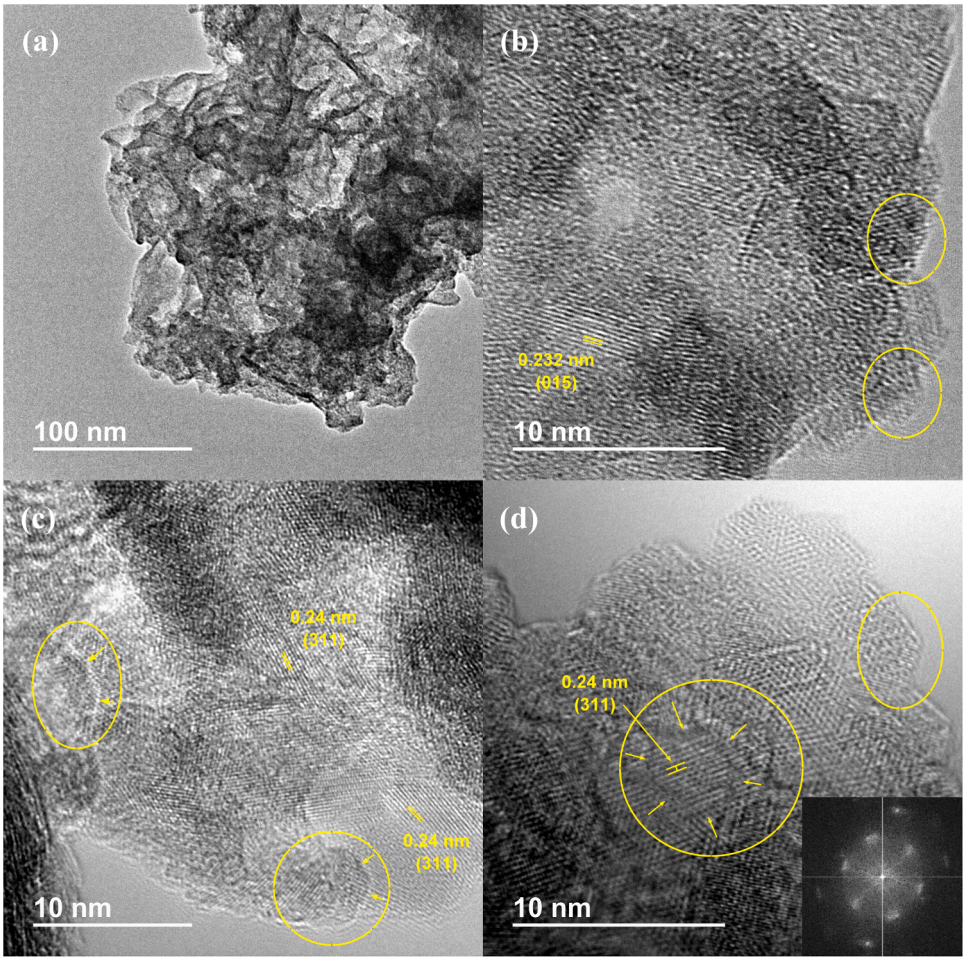

Fig. 2. TEM and HRTEM images of HE-LDH (a-b) and HE-MO (c-d). Electron diffraction pattern of HE-MO indicating its crystallinity at the nm scale is shown in Fig. 2d as an inset. Yellow arrows and circles in the images point at particle edges showing 120 ° angles, typical of hexagonal morphology of LDHs (images b-d). Lattice fringe distances and the corresponding XRD facet diffraction line have also been indicated in the high-resolution images of parts b and d.

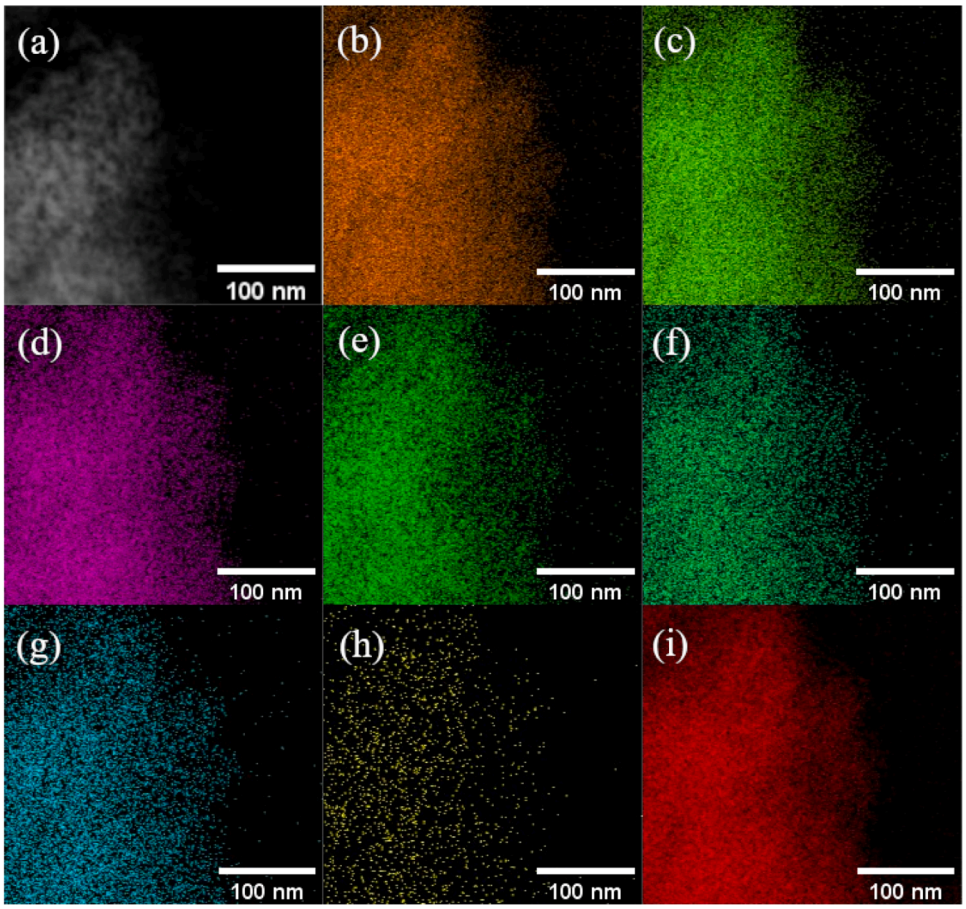

Fig. 3. HAADF-STEM image (a) and elemental distribution for Co (b), Zn (c), Mg (d), Fe (e), Al (f), Ga (g), In (h), and O (i) in HE-MO.

other groups[39]. For Fe $2p_{3/2}$, the XPS peak can be deconvoluted in two components at 711.3 and 713.3 eV, attributable to Fe^{3+} in different coordination environments. The satellite peak observed at 719.4 eV is characteristic of Fe in + 3 oxidation state[40]. For the XPS O 1 s peak, the experimental spectra could be deconvoluted in two components at 530.1 and 532.1 eV that can be attributed to lattice oxygen and oxygen vacancies and/or surface hydroxyl groups, respectively[41]. For the remaining metallic elements, experimental XPS peaks show typical configurations corresponding to the expected + 2 or + 3 oxidation states, according to the measured binding energy values[42,43].

In the case of CoFe mixed oxide, the higher ratio of both metals in the material allows a better observation of the high resolution XPS peaks. XPS of Co 2p peak shows two components at binding energy values of 779.7 and 781.1 eV attributable to Co atoms in different oxidation state [28]. For the XPS Fe $2p_{3/2}$ peak, two components at binding energy values of 709.7 and 711.2 eV were obtained from the best deconvolution of the XPS spectra attributable to Fe^{+3} ions in different coordination spheres[40]. XPS O 1 s peak has a mayor component at 529.7 eV attributable to lattice oxygen atoms accompanied by a minor component at 531.4 eV that most probably corresponds to oxygen vacancies or surface hydroxyl groups. Fig. S6 in supporting information present the survey XPS spectra and the high resolution XPS peaks for the control CoFe mixed oxide.

UV–visible absorption spectra of HE-MO recorded in the diffuse reflectance mode for the dry powders show a continuous absorption in the whole wavelength range with some absorption intensity increase towards the UV region. Accordingly, the Tauc plots considering both catalytic materials as indirect semiconductors show a narrow band gap of 1.53 eV and 1.33 eV for HE-MO and CoFe-MO, respectively. Fig. 4 also presents the diffuse reflectance absorption spectrum for HE-MO in comparison with that of CoFe mixed oxide. Importantly, the broad continuous absorption for HE-MO, and particularly, the absence of a defined absorption peak seems to indicate that no defined M ← O electronic transition occurs in the UV and visible regions.

3.2. Photocatalytic activity for nitrogen hydrogenation

Photocatalytic experiments were carried out under continuous flow using a 300 W Xe lamp that was illuminating a circular area (10 mm diameter) in which 50 mg of photocatalyst were deposited as a thin uniform bed. The gas flow consisted in 30 $ml{\cdot}min^{-1}$ of H_2 and 10 $ml{\cdot}min^{-1}$ of N_2 that were purified before entering the photoreactor by first flowing through a 0.5 mM aqueous solution of sulfuric acid to remove any NH_3 impurity in the feed, then through water and finally through $CaCl_2$ as desiccant. The flow was preheated at the required temperature before entering the photoreactor chamber, which was also heated at the same temperature. Measurements were conducted in the dark and under illumination from 100 to 350 ºC with temperature increments of 50 ºC. After the photocatalytic reaction, the gas flow was analyzed by flowing the stream through two consecutive trapping flasks containing 0.5 mM sulfuric acid. While the first sulfuric acid flask is supposed to trap all the ammonia formed in the photocatalytic reaction, the second trapping flask ensures that no ammonia has escaped to the absorption in the first flask. In fact, all the measurements trying to detect ammonia in the second trapping flask were negative, thereby confirming that the measurements in the first H_2SO_4 flask correspond to all NH_3 formed in the photocatalytic continuous flow reaction. The ammonia captured in the first flask after exiting the photoreactor was quantified by the indophenol method[31]. The employed calibration plot obtained using reference NH_3 samples is provided in Fig. S7a and the UV-Vis

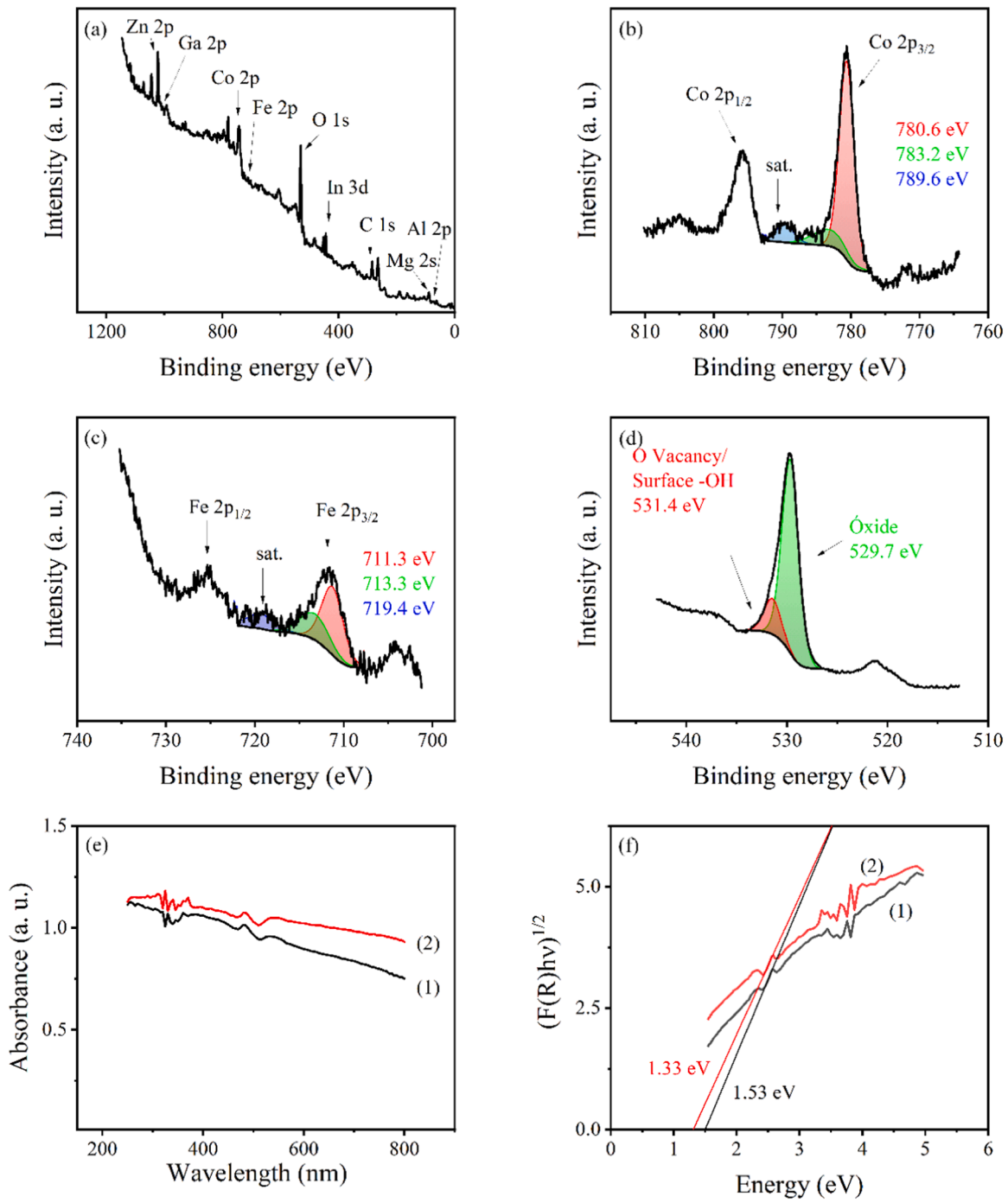

Fig. 4. Survey spectra showing the presence of seven metallic elements (a) and high resolution XPS of HE-MO: Co 2p peak (b), Fe 2p peak (c) and O 1 s peak (d). The plots also present the best deconvolution fitting of each XPS peak to individual components, including binding energy values and their assignment. UV-Vis DRS spectra (e) of HE-MO (1) and CoFe-MO (2). Tauc plot (f), including estimated band gap value, for HE-MO (1) and CoFe-MO (2).

absorption spectrum of the indophenol solution is given in Fig. S7b. Moreover, the blank test (no loaded catalyst in the photoreactor) verified that no ammonia was generated, ruling out any interference (Fig. S7c). No reaction products other than ammonia were detected in our experiments.

Fig. 5 shows the ammonia formation rate by collecting all the ammonia formed in 30 min in the range of temperature from 100 to 350 ºC, both in the dark and under irradiation. As it can be seen there, the ammonia production in the dark was much less than under illumination, reaching a maximum of 1.5 μmol $NH_3 \cdot g^{-1} \cdot h^{-1}$ at 150 ºC. Under UV–visible illumination, the maximum ammonia production of 20 μmol $NH_3 \cdot g^{-1} \cdot h^{-1}$ was achieved at 200 ºC. Under identical temperature and conditions in the dark, NH_3 production rate was less than one order of magnitude (below 1.5 μmol $NH_3 \cdot g^{-1} \cdot h^{-1}$).

One important observation was that a further increase in the reaction temperature above 200 ºC results in a significant decrease in ammonia formation. This observation of a maximum in ammonia rate as a function of the temperature suggests the operation of two opposite factors in the process. On one hand, an increase in the reaction temperature favors ammonia formation and this effect prevails up to 200 ºC. On the other hand, higher temperatures result in a transformation of the photocatalyst under the reaction conditions and this negative effect

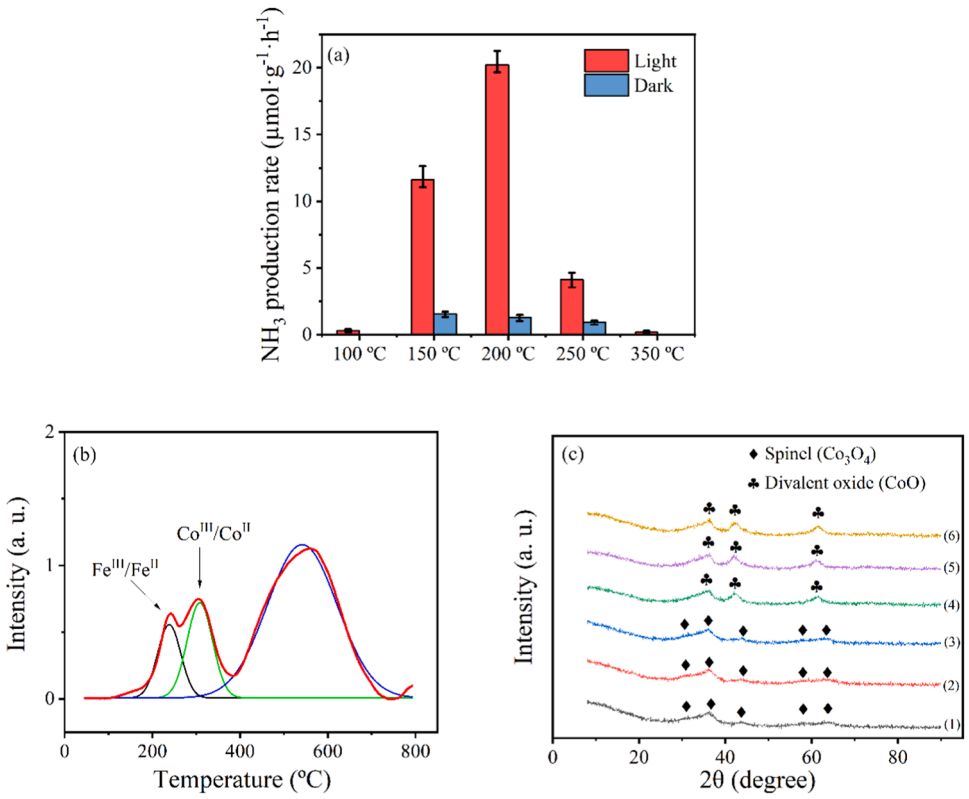

Fig. 5. a) NH_3 production rate in the photocatalytic N_2 hydrogenation over HE-MO at different temperatures (red) in comparison to the same conditions in the dark (blue). Reaction conditions: continuous gas flow (10 ml·min^{-1} N_2, 30 ml·min^{-1} H_2), UV-Vis irradiation (108 mW·cm^{-2}), 50 mg photocatalyst, temperature as indicated in the plot. b) H_2-TPR profile (red) of HE-MO and the three reduction maxima 240 (blue), 305 (green) and 550 (black) °C. c) PXRD profiles of HE-MO obtained under H_2 atmosphere (10 % in Ar, 60 ml·min^{-1}) at 25 ºC (1), 100 ºC (2), 200 ºC (3), 300 ºC (4), 400 ºC (5) and after cooling down the system to room temperature (6).

apparently prevails at temperatures higher than 200 ºC. This change in the photocatalyst could correspond to the formation of metal nanoparticles and segregation of different phases at higher temperatures, with the consequent loss of its high-entropy characteristics.

This proposal is supported by H_2-TPR measurement performed for HE-MO. Fig. 5b presents the H_2 consumption as a function of the temperature to which the photocatalyst is exposed. As it is observed in this Figure, two maxima for H_2 uptake appear at 240 and 305 ºC, attributable to the reduction of Fe^{3+} and Co^{3+} to their corresponding dipositive oxidation states, respectively. At temperatures above 600 ºC a bigger H_2 peak is measured due to the reduction of divalent cations to metallic state. These H_2-TPR measurements indicate that, at temperatures above 200 ºC, HE-MO starts to undergo a reduction process that should lead to profound phase changes from the initial photocatalytic material. The temperature range for the observation of the first H_2-TPR peak coincides with the decrease in the photocatalytic activity, so this interaction with H_2 appears to be the most reasonable explanation.

To gain more information about the transformation that HE-MO undergoes under the reaction conditions, an in-situ XRD study was performed in which the HE-MO was heated in the XRD probe under H_2 flow (10 % H_2 in Ar, 60 ml·min^{-1}), while the diffraction pattern is monitored at certain temperature intervals. A gradual change from the initial XRD corresponding to spinel cobaltite type phase with poor crystallinity towards a more crystalline divalent CoO-type metal oxide was observed, as indicated in Fig. 5c. Therefore, this transformation indicates that, above a certain temperature threshold, trivalent cations gradually undergo an in-situ reduction to form divalent species. The higher crystallinity of the resulting divalent metal oxide would be due to thermal annealing of the material at temperatures up to 300 ºC and a probable growth of particle size. These transformations are again in line with the previous explanation given to understand the decrease in the photocatalytic N_2 hydrogenation activity above certain temperatures. Upon increasing the temperature above 200 ºC, a change in the oxidation state of the metal ions and an annealing process take place, resulting in particles with higher crystallinity, larger sizes, and lower photocatalytic activity. These studies, in correlation with the obtained photocatalytic activity at different temperatures, support the hypothesis that the most active phase for N_2 hydrogenation is the high-entropy spinel-type structure, containing both divalent and trivalent cations, stable up to 200 ºC. At higher temperatures, when a phase transition process takes place, the photocatalytic activity diminishes.

Furthermore, the HE-MO sample was characterized after performing the N_2 hydrogenation at 200 ºC. XRD patterns of fresh and used HE-MO were comparable, no detecting any phase segregation (Fig. S8). HRTEM images of used HE-MO (Fig. S9) revealed the same particle size/shape as observed for the raw HE-MO in Fig. 2c, d, a layered-type morphology, also evidencing the lattice fringes of the (311) planes (0.242 nm), Fig. S9. Furthermore, the HAADF elemental mapping verified the even distribution of the 7 metal elements at the nanometric scale (Fig. S10).

XPS measurements performed after the photocatalytic test showed similar XPS peaks distribution and shapes, although a slight shift towards higher binding energy values can be observed in some of the metallic elements, as shown in Fig. S11. However, a more significant change is found in the O 1 s XPS peak (Fig. S12), where the relative intensity of the component at 531.6 eV, attributed to the surface hydroxyl groups and oxygen vacancies, increases. In addition, another component at 533.4 eV appears, attributable to structural water. These changes indicate that there is a hydration process taking place during the photocatalytic test, or that the material is more sensitive to hydration after being exposed to the test conditions. To further support the stability of the material, the NH_3 generated during the N_2 hydrogenation at 200 ºC by HE-MO was monitored during the last 10 min of reaction (i.

e. after stabilization of the NH_3 production), demonstrating that the NH_3 was continuously generated (Fig. S13).

To confirm N_2 as the source of the ammonia formed in the reaction, two experiments were carried out. In one of them, the photocatalytic process was conducted in the absence of N_2, under Ar atmosphere. Although NH_3 formation was detected even in the absence of N_2, the NH_3 formation rate was in the range of 0.3 μmol $NH_3 \cdot g^{-1} \cdot h^{-1}$, negligible when compared with the photocatalytic reaction performed in the presence of N_2, as seen in Fig. S14. This generated ammonia could be due to the presence of N_2 or NH_3 impurities in the gas feed and the reactor system, as it has been previously reported[44]. In a second experiment under batch conditions, labelled $^{15}N_2$ was used as substrate and the resulting $^{15}NH_3$ photoproduct was characterized by liquid ^1H NMR spectroscopy. Fig. 6 provides the ^1H NMR spectra recorded for $^{15}NH_3$ formed in the isotopic labelling experiment. As it can be seen in these spectra, the characteristic doublet coupling ($^1J_{15N\text{-}1H} = 73.17$ Hz) of ^{15}N ($^{15}NH_4^+$) is clearly recorded, whereas the triplet peaks of ^{14}N are detectable ($^1J_{14N\text{-}1H} = 52.22$ Hz), but very weak[45], therefore firmly confirming gaseous N_2 as the source of NH_3.

To provide some data showing the advantage of HE-MO as photocatalyst in comparison to bimetallic mixed oxides, an additional experiment was carried out using CoFe-MO obtained following an analogous procedure as the one employed here for the preparation of HE-MO. CoFe was selected in view of the activity of metals in thermal Haber-Bosch hydrogenation[46]. The results are presented in Fig. 6c. As it can be seen there, even though bimetallic CoFe oxide also affords NH_3 in a rate of 4 $\mu mol/g^{-1} \cdot h^{-1}$, this formation rate is five times smaller than for HE-MO. To deep into the photoresponse of these compounds, their transient photocurrents were recorded after depositing the compounds onto FTO glasses (Fig. S15a). The registered photocurrents are shown in Fig. S15b, where it was observed a higher intensity for the HE-MO sample compared to the CoFe oxide, which indicates a more efficient electron-hole separation in HE-MO.

Further comparison of the performance of multimetallic mixed oxide as photocatalyst for N_2 hydrogenation is provided by Table S2 in which a summary of literature data is provided. As can be seen there, the results achieved here compare favorably with those reported in the literature using noble metal-free photocatalysts, thereby showing the clear advantages of combining many metals to increase the photocatalytic activity of mixed oxides. According to this literature survey higher NH_3 production rates have been reported using Ru, sometimes promoted by Cs, at temperatures about 300 °C, or at 60 °C using an Au catalyst. Thus, our high entropy mixed oxide stands as one alternative to the use of precious or semiprecious metals for the reaction, highlighting the performance under continuous-flow mode, and the synthesis simplicity (coprecipitation followed by mild calcination at open air). The possible reasons for the performance enhancement of HE-MO should be related to the effective dilution of Co/Fe sites into the oxide structure, along with a possible positive effect derived from the contribution of the remaining metals.

3.3. Reaction mechanism

To gain information about the mechanism of the photocatalytic N_2 hydrogenation, two series of experiments keeping constant the flow of one of the reagents and varying the flow of the other in the range from 5 to 40 $ml \cdot min^{-1}$ were carried out. Fig. S16 in supporting information presents the NH_3 formation rate as a function of the composition of the gas feed. It was observed that keeping constant N_2 flow, an increase of H_2 flow enhances NH_3 formation rate. In contrast, an analogous

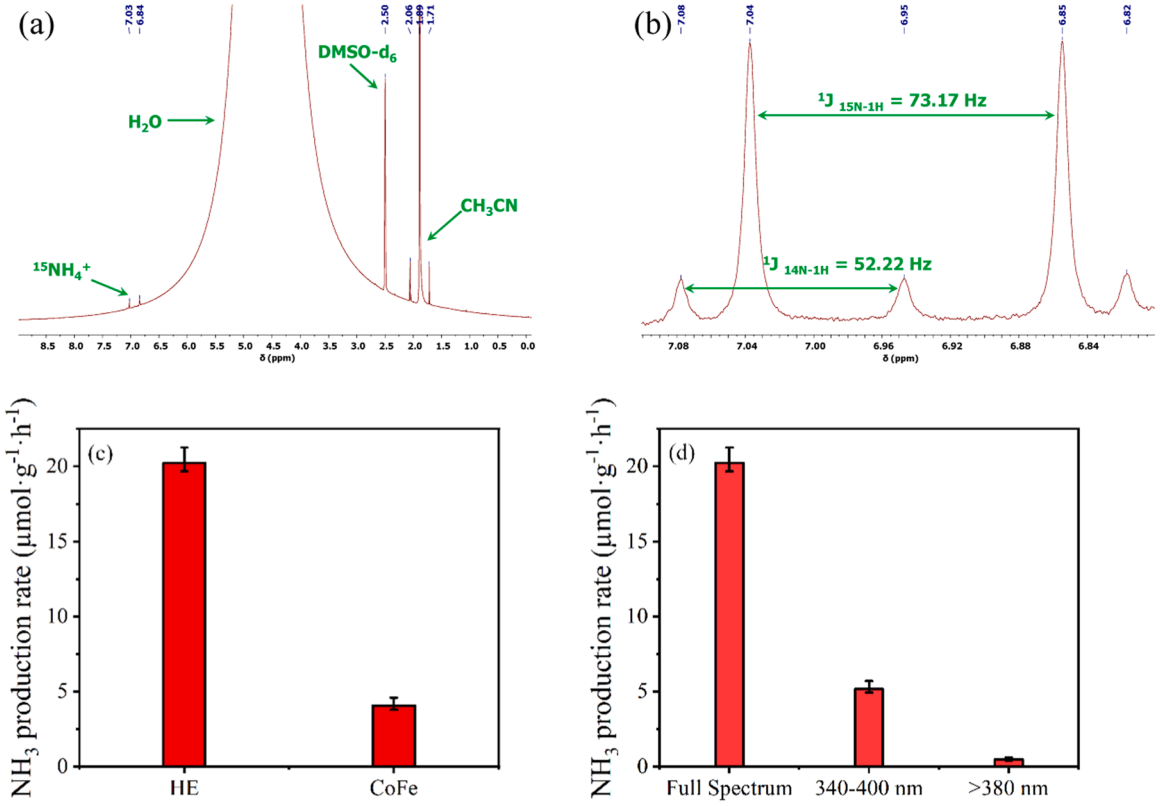

Fig. 6. (a) Complete ^1H NMR spectrum and (b) its enlargement for the ambient pressure $^{15}N_2$ hydrogenation using HE-MO as photocatalysts. DMSO-d_6 and CH_3CN were used as reference and internal standard, respectively. Reaction conditions: full output of a Xe lamp (108 $mW \cdot cm^{-2}$), feed: $^{15}N_2/H_2$ (1/3), temperature 200 °C, HE-MO 50 mg, reactor volume 51 ml, irradiation time 90 h. (c) Comparison of the activity in photocatalytic N_2 hydrogenation between HE-MO and CoFe-MO. (d) Influence of irradiation wavelength on the activity of HE-MO for photocatalytic N_2 hydrogenation. Reaction conditions: continuous flow (10 $ml \cdot min^{-1}$ N_2, 30 $ml \cdot min^{-1}$ H_2), T: 200 ºC, UV–vis irradiation (without filter, with band-pass filter at 340–400 nm, or with cut-off filter at 380 nm), 50 mg photocatalyst.

experiment keeping constant the H_2 flow shows that an increase in the N_2 flow decreases NH_3 formation rate. This indicates that H_2 adsorption and activation on the surface of HE-MO is the rate determining step in NH_3 formation. In that way, if the relative H_2 concentration increases, more H_2 derived active species should be on the photocatalyst surface, thereby increasing NH_3 formation rate. On the contrary, competition of N_2 for the adsorption sites on the photocatalyst surface disfavors NH_3 formation.

The response of the photocatalyst was studied by comparing the activity upon irradiation through quartz with the full output of a Xe lamp with the activity after filtering the visible and NIR irradiation or using a range of wavelengths. The results are presented in Fig. 6d. It was observed that the photoresponse upon irradiation at wavelengths longer than 380 nm is almost negligible, meaning that the photocatalytic response is due to UV excitation of HE-MO. This is confirmed by using a band-pass filter with nominal wavelengths in the range between 340 and 400 nm and observing a rate NH_3 formation of 5 μmol $g^{-1}{\cdot}h^{-1}$. This NH_3 formation rate is approximately proportional to the total UV photons irradiating the photocatalyst (a factor about 3.4), thus confirming that any wavelength shorter than 380 nm is equally efficient to promote NH_3 formation.

This result, however, confront with the optical absorption spectrum of the HE-MO that absorbs almost equally in the full range of UV, visible and NIR radiations. To reconcile these opposite pieces of evidence it has to be admitted that the fact that only the UV-region results in NH_3 formation should correspond to the existence of certain electronic transitions with sufficient energy to promote the reaction. The existence of these electronic transitions in the UV region was supported by photoluminescence measurements. Thus, a scanning of the emission spectra of HE-MO exciting with wavelengths in the range 300–400 nm was performed. In all of the obtained spectra, a photoluminescence emission peak at 445 nm was observed, achieving the maximum intensity when excitation was made at 350 nm (see Fig. 7). Observation of this emission indicates that upon photon absorption in the UV region a photoinduced charge separation state with generation of electrons and holes is generated. Radiative charge recombination of these transient states can occur, resulting in the emission of a detectable photon. It is proposed that these transient states responsible for the photoluminescence are also responsible for the photocatalytic activity. This behavior has been previously observed in low band gap metal oxides containing several metallic elements in a spinel-type structure[47].

To support this hypothesis, the band structure of the photocatalytic materials in the present work was studied by valence band XPS and UPS, and the results are shown in Fig. S17 and S18. It was found that both photocatalysts display p-type semiconductor behavior, as the Fermi level was closer to the corresponding valence band (VB). Remarkably, it can be noted that the VB of HE-MO is located at more negative potentials compared to CoFe-MO. Although the potentials of the conduction band (CB) of both photocatalysts are not negative enough to achieve the theoretical values for N_2 activation displayed in Fig. S19, the more negative potential of HE-MO CB should lower the energy requirements of the incident UV photons to achieve certain potential above the CB, responsible for the photocatalytic N_2 hydrogenation activity. This is in agreement with the experimental results showing a higher activity for HE-MO compared to CoFe-MO. In addition, it has been reported that the photoexcited electrons on the surface of the photocatalytst can be transferred into an anti-bonding orbital of strongly chemisorbed N_2, which weakens the N_2 triple bond and eventually unlocks NH_3 production[48,49]. Furthermore, the measurement of the TRPL decay (Fig. S20) was performed to evaluate the photocharge lifetime of HE-MO. Instrument Response Function (IRF) was also measured to check the response time of the excitation/detection. The obtained curve was better fitted to a bi-exponential function, yielding two lifetimes of $\tau1 = 0.88$ ns and $\tau2 = 3.48$ ns, indicating short times (nanosecond scale) for the generated photocharges.

4. Conclusions

As a highly relevant finding, the present study has shown the formation of an LDH-derived mixed oxide with seven metals and its application in a photocatalytic reaction. This result is highly remarkable since LDH synthesis is mostly limited to the combination of two, three or maybe four metals. This opens new avenues in LDH synthesis to explore a vast chemical space of metal compositions. Also equally remarkable is that LDH transformation results in bidimensional HE-MO sheets with hexagonal morphology inherited from the precursor. The obtained evidence shows that no phase separation occurs as assessed either by XRD or electron microscopy. The potential of these multimetallic HE-MOs can be very large considering that bimetallic mixed oxides exhibit improved performance compared to monometallic oxides in many applications, going from catalysis, electrocatalysis, photocatalysis, to other areas such as supercapacitors and energy storage. In the present study we have shown that an HE-MO with seven metals, even without composition optimization, performs much better in the photocatalytic N_2 hydrogenation than bimetallic mixed oxides and other noble metal-free photocatalysts reported in the literature. Further progress in this area will be theory driven selection of the transition metals in optimal proportions within the limits allowed in LDH synthesis. Thus, further work continuing this present finding could provide unprecedented, advanced oxides with optimal properties respect to the existing ones.

CRediT authorship contribution statement

Hermenegildo García: Writing – review & editing, Supervision. **Adrián Pastor:** Writing – original draft, Investigation, Data curation. **Manuel Molina-Muriel:** Writing – original draft, Investigation, Data

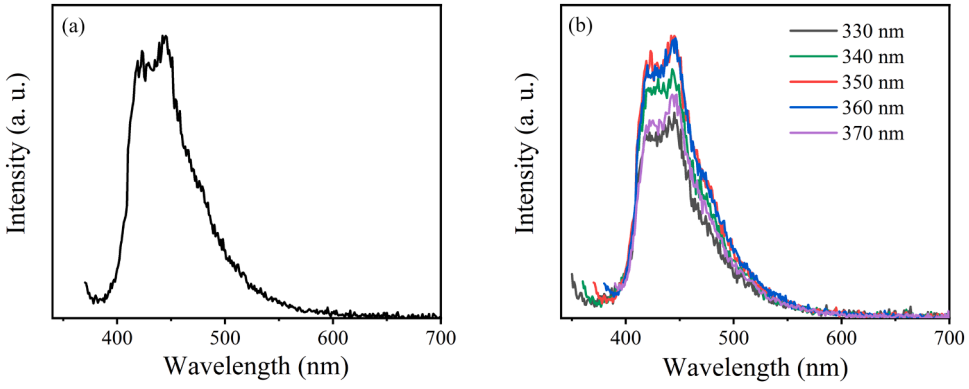

Fig. 7. Steady state photoluminescence emission spectrum of HE-MO upon excitation at 350 nm (a). Variation on the emission intensity upon excitation at different excitation wavelengths (b).

curation. **Antonio Ribera:** Writing – review & editing, Supervision. **Fernando Déniz:** Investigation, Data curation.

Declaration of Competing Interest

The authors declare that they have no known competing financial interests or personal relationships that could have appeared to influence the work reported in this paper.

Acknowledgements

Financial support by the Spanish Ministry of Science and Innovation and Universities (CEX-2021–001230-S, PDI2021-0126071-OB-CO21 and PID2021-125907NB-I00 funded by MCIN/AEI/ 10.13039/501100011033/FEDER) and Generalitat Valenciana (Prometeo 2021/038, CIPROM-2022-60 and Advanced Materials programme Graphica MFA/2022/023 and MFA-2022-057 with funding from European Union Next Generation EU PRTR-C17.I1) are gratefully acknowledged. Adrián Pastor acknowledges the Margarita Salas postdoctoral fellowship, within the Recovery, Transformation and Resilience Plan (Spanish Ministry of Science, Innovation and Universities), funded by the European Union Next GenerationEu. Manuel Molina-Muriel thanks the Universitat Politècnica de València for a postgraduate scholarship. The authors acknowledge Francisco De Paula Martín for his support regarding the UPS and VB-XPS measurements.

Appendix A. Supporting information

Supplementary data associated with this article can be found in the online version at doi:10.1016/j.jece.2025.117541.

Data availability

Data will be made available on request.

References

[1] U. Farooq, T. Ahmad, F. Naaz, Su Islam, Energy Fuels 37 (2023) 1577–1632, https://doi.org/10.1021/acs.energyfuels.2c03396.
[2] P. Wang, R. Shi, J. Zhao, T. Zhang, Adv. Sci. (2023) 2305471, https://doi.org/10.1002/advs.202305471.
[3] M.M. Nair, A.C. Iacoban, F. Neaţu, M. Florea, J.Mater Neaţu, Chem.A 11 (2023) 12559–12592, https://doi.org/10.1039/D2TA08983A.
[4] S. Ali, J. Abdul Nasir, R. Nasir Dara, Z. Rehman, Inorg. Chem. Commun. 145 (2022) 110011, https://doi.org/10.1016/j.inoche.2022.110011.
[5] Y. Li, W. Su, Y. Yang, L. Bai, J. Lu, W. Zhang, et al., Appl. Catal. B Environ. 341 (2024) 123282, https://doi.org/10.1016/j.apcatb.2023.123282.
[6] G. Qian, W. Lyu, X. Zhao, J. Zhou, R. Fang, F. Wang, et al., Angew.Chem.Int.Ed 61 (2022) e202210576, https://doi.org/10.1002/anie.202210576.
[7] F. Chen, L. Zhou, C. Peng, D. Zhang, L. Li, D. Xue, et al., Appl. Catal. B Environ. 331 (2023) 122689, https://doi.org/10.1016/j.apcatb.2023.122689.
[8] M.M. Islam, T. Bredow, J. Phys. Chem. C. 119 (2015) 5534–5541, https://doi.org/10.1021/acs.jpcc.5b00023.
[9] W. Deng, Q. Tang, S. Huang, L. Zhang, Z. Jia, L. Guo, Appl. Catal. B Environ. 278 (2020) 119336, https://doi.org/10.1016/j.apcatb.2020.119336.
[10] Z. Li, Q. Yan, Q. Jiang, Y. Gao, T. Xue, R. Li, et al., Appl. Catal. B Environ. 269 (2020) 118827, https://doi.org/10.1016/j.apcatb.2020.118827.
[11] Y. Xu, Z. Wang, L. Tan, Y. Zhao, H. Duan, Y. Song, Ind. Eng. Chem. Res 57 (2018) 10411–10420, https://doi.org/10.1021/acs.iecr.8b02246.
[12] W. Li, P. Hou, Z. Wang, P. Kang, Sustain. Energy Fuels 3 (2019) 1455–1460, https://doi.org/10.1039/C9SE00056A.
[13] Z. Peng, C. Yang, Y. Hu, F. Bai, W. Chen, R. Liu, et al., Appl.Surf.Sci 573 (2022) 151561, https://doi.org/10.1016/j.apsusc.2021.151561.
[14] V.I. Popkov, V.P. Tolstoy, V.G. Semenov, J.Alloys Compounds 813 (2020) 152179, https://doi.org/10.1016/j.jallcom.2019.152179.
[15] Z.W. Chen, J. Li, P. Ou, J.E. Huang, Z. Wen, L. Chen, et al., Nat. Commun. 15 (2024) 359, https://doi.org/10.1038/s41467-023-44261-4.
[16] X. Xu, W. Yang, H. Song, J. Wang, L. Yu, Z. Ren, et al., Scr.Mater 243 (2024) 115986, https://doi.org/10.1016/j.scriptamat.2024.115986.
[17] Y. Pan, J. Liu, T. Tu, W. Wang, G. Zhang, Chem.Eng.J 451 (2023) 138659, https://doi.org/10.1016/j.cej.2022.138659.
[18] A. Amiri, R. Shahbazian-Yassar, J. Mater. Chem. A 9 (2021) 782–823, https://doi.org/10.1039/D0TA09578H.
[19] Y. Gao, Y. Liu, H. Yu, D. Zou, Appl. Catal. A Gen. 631 (2022) 118478, https://doi.org/10.1016/j.apcata.2022.118478.
[20] M. Fracchia, M. Coduri, P. Ghigna, U. Anselmi-Tamburini, J. Eur. Ceram. Soc. 44 (2024) 585–594, https://doi.org/10.1016/j.jeurceramsoc.2023.09.056.
[21] X. Yu, B. Wang, C. Wang, C. Zhuang, Y. Yao, Z. Li, et al., Small 17 (2021) 2103412, https://doi.org/10.1002/smll.202103412.
[22] A.J. Knorpp, A. Zawisza, S. Huangfu, A. Borzì, A.H. Clark, D. Kata, et al., RSC Adv. 12 (2022) 26362–26371, https://doi.org/10.1039/D2RA05435C.
[23] T.X. Nguyen, C. Tsai, V.T. Nguyen, Y. Huang, Y. Su, S. Li, et al., Chem.Eng.J 466 (2023) 143352, https://doi.org/10.1016/j.cej.2023.143352.
[24] F. Cavani, F. Trifirò, A. Vaccari, Catal. Today 11 (1991) 173–301, https://doi.org/10.1016/0920-5861(91)80068-K.
[25] M. Molina-Muriel, Y. Peng, H. García, A. Ribera, J. Alloy. Compd. 897 (2022) 163124, https://doi.org/10.1016/j.jallcom.2021.163124.
[26] J. Zhao, R. Shi, G.I.N. Waterhouse, T. Zhang, Nano Energy 102 (2022) 107650, https://doi.org/10.1016/j.nanoen.2022.107650.
[27] M. Kim, I. Oh, H. Choi, W. Jang, J. Song, C.S. Kim, et al., Cell Rep. Phys. Sci. 3 (2022) 100702, https://doi.org/10.1016/j.xcrp.2021.100702.
[28] X. Liu, X. Wang, B. Yang, J. Zhang, J. Lu, Nano Res. 16 (2023) 4775–4785, https://doi.org/10.1007/s12274-022-5259-5.
[29] W. Li, G. Zhao, J. Zhong, J. Xie, Fuel 358 (2024) 130155, https://doi.org/10.1016/j.fuel.2023.130155.
[30] J. Yu, B.R. Martin, A. Clearfield, Z. Luo, L. Sun, Nanoscale 7 (2015) 9448–9451, https://doi.org/10.1039/C5NR01077B.
[31] N.M. Tzollas, G.A. Zachariadis, A.N. Anthemidis, J.A. Stratis, Int. J. Environ. Anal. Chem. 90 (2010) 115–126, https://doi.org/10.1080/03067310902962528.
[32] H. Wu, J. Zhang, Q. Lu, Y. Li, R. Jiang, Y. Liu, et al., ACS Appl.Mater.Interfaces 15 (2023) 38423–38432, https://doi.org/10.1021/acsami.3c05781.
[33] X. Zhang, Y. Zhao, Y. Zhao, R. Shi, G.I.N. Waterhouse, T. Zhang, Adv. Energy Mater. 9 (2019), https://doi.org/10.1002/aenm.201900881.
[34] V. Rives, Mater. Chem. Phys. 75 (2002) 19–25, https://doi.org/10.1016/S0254-0584(02)00024-X.
[35] Y. Zhao, X. Jia, G. Chen, L. Shang, G.I.N. Waterhouse, L. Wu, et al., J.Am.Chem.Soc 138 (2016) 6517–6524, https://doi.org/10.1021/jacs.6b01606.
[36] P.J. Sideris, U.G. Nielsen, Z. Gan, C.P. Grey, Science 321 (2008) 113–117, https://doi.org/10.1126/science.1157581.
[37] K. Gu, X. Zhu, D. Wang, N. Zhang, G. Huang, W. Li, et al., J. Energy Chem. 60 (2021) 121–126, https://doi.org/10.1016/j.jechem.2020.12.029.
[38] G. Abellan, E. Coronado, C. Marti-Gastaldo, E. Pinilla-Cienfuegos, A. Ribera, J. Mater. Chem. 20 (2010) 7451–7455, https://doi.org/10.1039/c0jm01447h.
[39] R.D.S. Macedo, R. Boni Fazzi, A.M. da Costa Ferreira, V.R.L. Constantino, N. J. Chem. 44 (2020) 10022–10032, https://doi.org/10.1039/D0NJ00380H.
[40] M.C. Biesinger, B.P. Payne, A.P. Grosvenor, L.W.M. Lau, A.R. Gerson, R.S.C. Smart, Appl. Surf. Sci. 257 (2011) 2717–2730, https://doi.org/10.1016/j.apsusc.2010.10.051.
[41] M.C. Biesinger, B.P. Payne, L.W.M. Lau, A. Gerson, R.S.C. Smart, Surf. Interface Anal. 41 (2009) 324–332, https://doi.org/10.1002/sia.3026.
[42] Z.M. Detweiler, S.M. Wulfsberg, M.G. Frith, A.B. Bocarsly, S.L. Bernasek, Surf. Sci. 648 (2016) 188–195, https://doi.org/10.1016/j.susc.2015.10.026.
[43] M.C. Biesinger, L.W.M. Lau, A.R. Gerson, R.S.C. Smart, Appl. Surf. Sci. 257 (2010) 887–898, https://doi.org/10.1016/j.apsusc.2010.07.086.
[44] Y. Xiong, B. Li, Y. Gu, T. Yan, Z. Ni, S. Li, et al., Nat. Chem. 15 (2023) 286–293, https://doi.org/10.1038/s41557-022-01088-8.
[45] J. Liu, M.S. Kelley, W. Wu, A. Banerjee, A.P. Douvalis, J. Wu, et al., Proc. Natl. Acad. Sci. 113 (2016) 5530–5535, https://doi.org/10.1073/pnas.1605512113.
[46] J. Humphreys, R. Lan, S. Tao, Adv. Energy Sustain. Res 2 (2021) 2000043, https://doi.org/10.1002/aesr.202000043.
[47] M. Molina-Muriel, Y. Peng, H. Szalad, A. Ribera, H. García, J. CO2 Util. 81 (2024) 102725, https://doi.org/10.1016/j.jcou.2024.102725.
[48] Y. Zhao, Y. Zhao, G.I.N. Waterhouse, L. Zheng, X. Cao, F. Teng, et al., Adv. Mater. 29 (2017) 1703828, https://doi.org/10.1002/adma.201703828.
[49] Y. Zhao, L. Zheng, R. Shi, S. Zhang, X. Bian, F. Wu, et al., Adv. Energy Mater. 10 (2020) 2002199, https://doi.org/10.1002/aenm.202002199.